Supporting Information

Dispersion Mapping in 3-Dimensional Core-Shell Photonic Crystal Lattices Capable of Negative Refraction in the Mid-Infrared

Victoria F. Chernow, [†,⊥] *Ryan C. Ng,* [*,‡,§,⊥] *Siying Peng,* [†,||] *Harry A. Atwater,* [†] *Julia R. Greer*[†]

[†]Division of Engineering and Applied Sciences, California Institute of Technology, Pasadena, CA 91125, United States

[‡]Division of Chemistry and Chemical Engineering, California Institute of Technology, Pasadena, CA 91125, United States

Exploring Varied Simulation Parameters

Here, we investigate the effect of the variation of various parameters such as effective index of refraction, beam ellipticity, and shell-to-core position offset on AANR. We previously explored the effects of the fill fraction (i.e. volume fraction/beam diameter) and the effective index of refraction for polymer-Ge core-shell and carbon-Ge core-shell structures on AANR in PWE simulations, and now expand that analysis.[1]

***Effective Index of Refraction - Polymer Core, Si Shell PhCs*:** Another relatively high index dielectric material commonly utilized in PhC fabrication is silicon (n = 3.4189 at λ = 8.0 μm). Silicon deposition methods are more ubiquitous and better optimized compared to Ge deposition, so we also study the effect on average AANR frequency and frequency range when core-shell lattices are composed of polymer cores and Si shells. A summary of band structure and EFC simulations for such structures are summarized in Table S1. Similar to the case for polymer-Ge and carbon-Ge core-shell structures, we observe a monotonic increase in the average frequency for AANR and a monotonic decrease in AANR frequency range with decreasing compound refractive index of lattice beams (Figure S1(a-b)). As the diameter size of the polymer core increases and Si shell thickness decreases, the combined index of the whole PhC lowers and reaches a threshold index below which AANR is no longer possible. Specifically, by simulating EFCs, we again observe that below an index of n ~ 3.1, approximately equal to a polymer core of b_{core} = 400 nm and germanium shell of t_{shell} = 300 nm in lattices of volume fraction f = 0.23, an AANR region does not exist. As was the case with polymer-Ge core-shell lattices, below an index of 3.1, the periodic modulation effect is too weak, and EFCs change shape from circular to square-like. Figure 31(c) shows the band 3 EFCs for a lattice with b_{core} = 500 nm and t_{shell} = 250 nm, where n_{beam} = 2.94, showing that in the frequency region below the light line (which falls at ω =

0.520($2\pi c/a$) for this lattice) the contours have a square-like shape. Square-like EFCs imply that these lattices are capable of self-collimation but not do not display AANR, when the compound index of the PhC beams are below 3.1, irrespective of the materials comprising the structure (Si versus Ge).

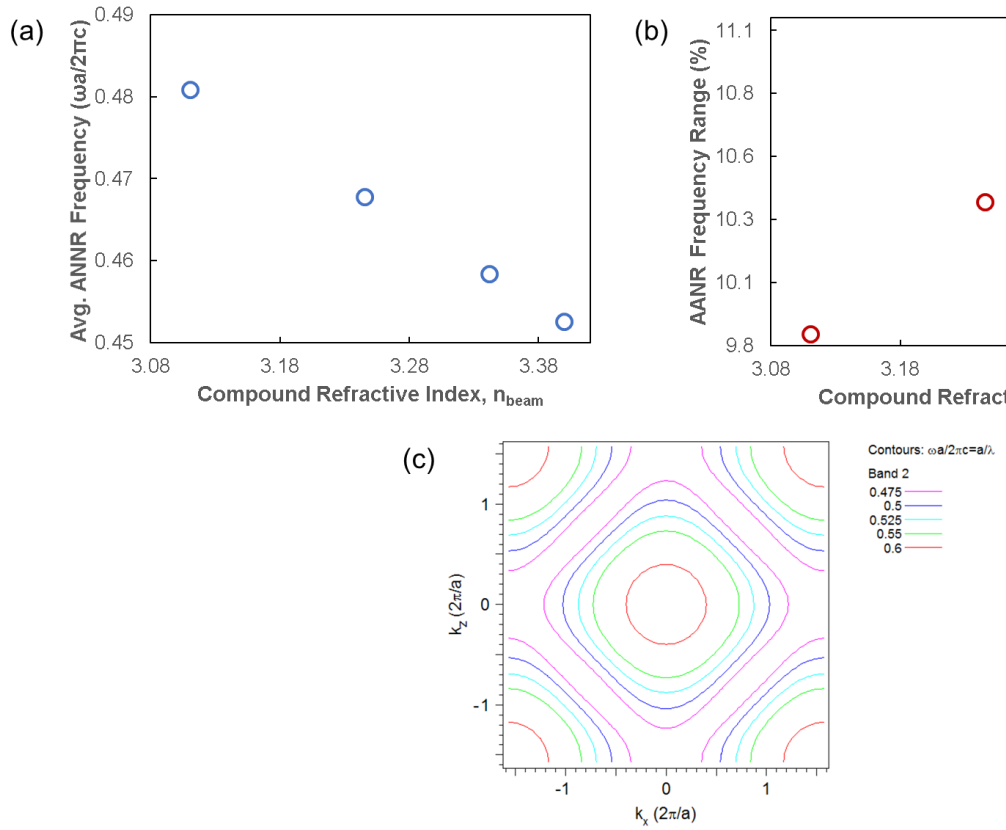

Figure S1. Average AANR Frequency, AANR Frequency range, and equi-frequency contours for polymer-silicon core-shell PhCs. (a) Average AANR frequency in the PhC when the compound refractive index of the lattice is varied (polymer core to Si shell ratio changes). (b) AANR frequency range, represented as a percentage difference, for PhCs with varying compound refractive index (polymer core to Si shell ratio changes). (c) Slice of the equi-frequency surfaces on the $k_y = 0$ plane for a PhC lattice with b_{core} = 500 nm and t_{shell} = 250 nm (n_{beam} = 2.94).

Table S1. Figures of merit derived from band structure and EFC calculations on core-shell PhC lattices of varied polymer core diameter and Si shell thickness.

Core beam diameter, b_{core} (μm)	Shell thickness, t_{shell} (μm)	Refractive Index, n_{beam}	Absolute Frequency Range, Δω (2πc/a)	Average AANR Frequency (2πc/a)	AANR Frequency Range (%)	Average AANR Wavelength (μm)
0.1	0.45	3.3996	0.0494	0.4526	10.9036	8.8376

0.2	0.40	3.3417	0.0491	0.4584	10.7066	8.7258
0.3	0.35	3.2453	0.0485	0.4678	10.3692	8.5498
0.4	0.30	3.1103	0.0474	0.4809	9.8474	8.3182

Because AANR with polymer-Si core-shell structures necessitates a circular core diameter on the order of 400nm, which is too small to achieve reliably with TPL DLW, we instead decided to pursue polymer-Ge core-shell designs, though pyrolysis could enable dimensions in which such a structure that exhibits AANR with a Si shell would be possible.

The Effect of Beam Ellipticity: From previous parameter sweeps, we identified that a volume fraction of $f = 0.23$, which translates to a circular beam diameter of 1.0 μm for a lattice with 4.0 μm periodicity, is appropriate for the fabrication of low index core, high index shell lattice structures with AANR in the mid-infrared (7.7-8.62 μm range). Specifically, we can aim to fabricate lattices with a 500 nm diameter polymer core, and 250nm germanium shell, which should display AANR between 8.4 μm - 9.41 μm. While these parameters provide useful guidelines for fabricating the desired core-shell nanolattice PhCs, it is not realistically possible to fabricate beams with perfectly circular cross-sections, as the volumetric pixel, or voxel, that is the building block of the TPL DLW process is inherently elliptically shaped. While specialized writing schemes can be employed to generate beams that are largely circular in cross-section (see reference 2 for more details), fabricated beams will possess some degree of elliptical shape. To quantify the effect on average AANR frequency and frequency range when the cross-section of core-shell beams becomes increasingly elliptical, we calculated band structure and EFCs varying the parameter of ellipticity, ξ, while keeping cross-sectional area of beams constant (both full beam cross-sectional area and respective core and shell cross-sectional areas are kept constant) for a lattice with a polymer core of $b_{core} = 500$ nm and germanium shell of $t_{shell} = 250$ nm.

Ellipticity is a measure of the compression of a circle along a diameter to form an ellipse, and can be defined as $\xi = \frac{a-b}{a}$, where a is the dimension of the semi-major axis of the total beam, and b is the dimension of the semi-minor axis of the beam. We varied the semi-major axis from a = 0.5 μm to $a = 0.83\overline{3}$ μm, and the semi-minor axis, which was treated as a function of a, varied from $b = 0.5^2/a$ = 0.5 μm to 0.3 μm. In this manner, beam cross-sectional area was kept constant at 0.785 μm^2, while ellipticity varied from $\xi = 0$, for a circular cross-section, to a maximum of ξ = 0.64 (Table S2).

Table S2. Figures of merit derived from band structure and EFC calculations on core-shell PhC lattices with beams of varying ellipticity and constant cross-sectional area.

Semi-major beam axis, a (μm)	Semi-minor beam axis, b (μm)	Ellipticity, $\xi\left(\frac{a-b}{a}\right)$	Absolute Frequency Range, Δω (2πc/a)	Average AANR Frequency (2πc/a)	AANR Frequency Range (%)	Average AANR Wavelength (μm)
0.5	0.5	0	0.0509	0.4507	11.3048	8.8753
0.5556	0.45	0.19	0.0494	0.4531	10.9054	8.8286
0.625	0.4	0.36	0.0479	0.4567	10.4933	8.7586
0.7143	0.35	0.51	0.0461	0.4629	9.9654	8.6415
0.8333	0.3	0.64	0.0446	0.4712	9.4696	8.4893

As the beam ellipticity increases, we observe a monotonic increase in the average frequency for AANR, and a monotonic decrease in AANR frequency range (Figure S2(a-b)). This is the result of bands compressing, and band 3 specifically shifting to higher frequencies as beams become more elliptical in shape. Figure S2(c-d) shows the actual band structure in the Γ-N direction for varying ξ. While the relative shape or concavity of band 3 does not change with ξ, we witness a decrease in band separation between bands 3 and 4, as well as a migration of band 3 to higher frequencies with increasing ellipticity.

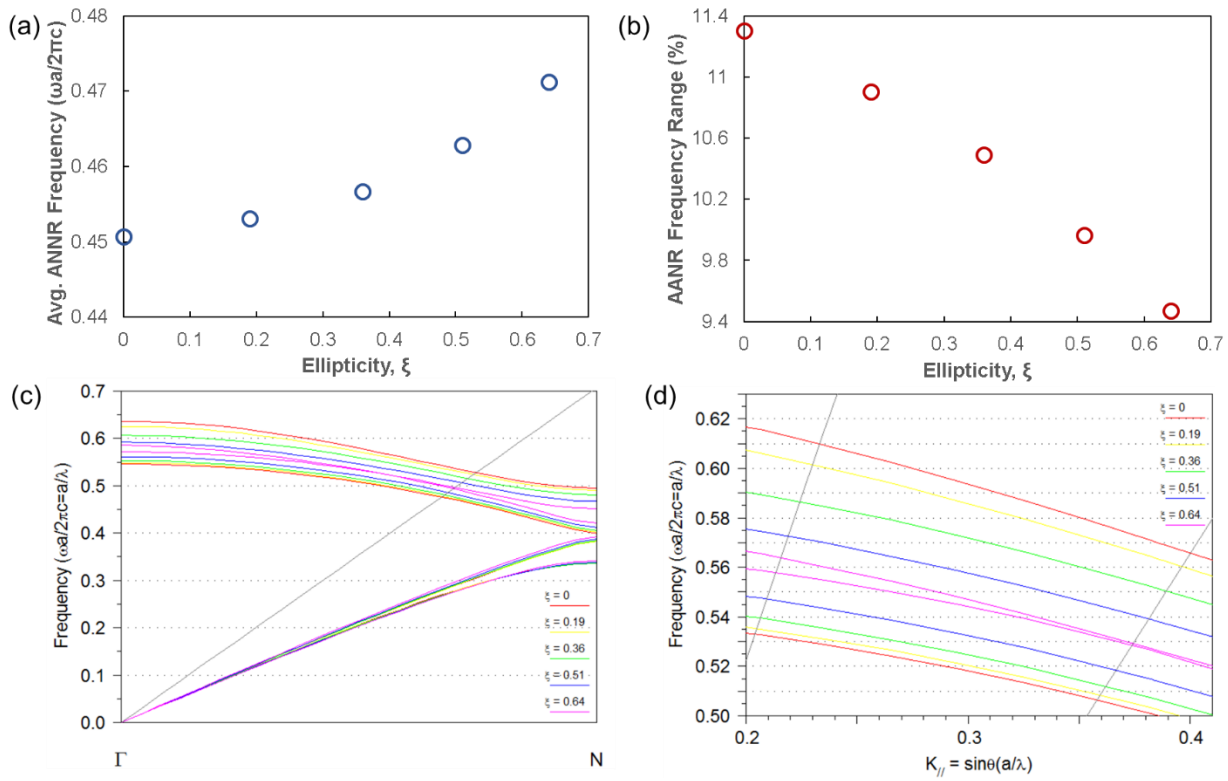

Figure S2. Average AANR Frequency, AANR Frequency range, and evolution of band structure for polymer-germanium core-shell PhCs with beams of varying ellipticity. (a) Average AANR frequency in the PhC when beam ellipticity is varied (ratio of lattice beam semi-major and semi-minor axes changes). (b) AANR frequency range, represented as a percentage difference, for PhCs with varying beam ellipticity. (c) Band structure along the Γ*N* direction for the 3D core-shell PhC with varying beam ellipticity. The grey diagonal line is the light line (90° relative to the surface normal). (d) An enlarged subset of the band structure presented in *(c)*. The grey diagonal lines denote the angular span between 22.5° and 45°.

The Effect of Shell Offset Relative to Core Position: The process of creating core-shell lattice structures will involve deposition of high-index germanium onto low index polymer scaffolds. If Ge deposition is conformal but anisotropic, we can approximate beam cross-sections as "egg-yolks," where the Ge shell position is offset from the center position of the polymer core, as depicted in Figure S3(a). We study the effect of Ge shell offset on average AANR frequency and frequency range by simulating 500nm polymer core, 250nm Ge shell lattices and displacing the center position of the Ge shell relative to the polymer core center from 0 to 250nm in one

dimension, the X-direction, two dimensions, the X and Z-directions (Ge shell is offset from the polymer core center by 0 to 250nm in both the X and Z directions), and in all three dimensions, the X-Y-Z-directions (Figure S3(a)). We perform band structure and EFC simulations for all three offset varieties, and report the figures of merit in Table S3.

Table S3. Figures of merit derived from band structure and EFC calculations on polymer-Ge core-shell PhC lattices with Ge shell offset from the center core position in the X-direction, XZ-directions, and XYZ-directions.

Offset Type	Offset Value (μm)	Absolute Frequency Range, Δω (2πc/a)	Average AANR Frequency (2πc/a)	AANR Frequency Range (%)	Average AANR Wavelength (μm)
X-offset	0	0.0509	0.4507	11.3045	8.8752
	0.05	0.0515	0.4493	11.4605	8.9037
	0.1	0.0521	0.4471	11.6452	8.9471
	0.15	0.0526	0.4445	11.8365	8.9995
	0.2	0.0531	0.4417	12.0104	9.0556
	0.25	0.0533	0.4392	12.1378	9.1075
XZ-offset	0	0.0509	0.4507	11.3045	8.8752
	0.05	0.0510	0.4495	11.3466	8.8990
	0.1	0.0507	0.4475	11.3212	8.9388
	0.15	0.0500	0.4451	11.2231	8.9865
	0.2	0.0490	0.4425	11.0718	9.0392
	0.25	0.0479	0.4394	10.8989	9.1030
XYZ-offset	0	0.0509	0.4507	11.3045	8.8752
	0.05	0.0503	0.4492	11.2058	8.9042
	0.1	0.0486	0.4473	10.8718	8.9433
	0.15	0.0461	0.4451	10.3610	8.9864
	0.2	0.0435	0.4422	9.8432	9.0454
	0.25	0.0425	0.4359	9.7517	9.1769

We observe that, as the degree of offset increases in all three tests, average AANR frequency monotonically decreases, and the value of average AANR frequency does not vary significantly

between samples offset in X, XZ, and XYZ (Figure S3(b)). This is because in general, offsetting the Ge shell from the center of the polymer core shifts the position of AANR relevant band 3 to smaller frequencies. In comparison, the degree of offset has a more complex effect on AANR frequency range (Figure S3(c)). Increasing the degree of X-offset appears to increase AANR frequency range, while increasing XZ and XYZ-offset lowers the AANR frequency range. These trends are the result of the offset parameter subtly changing the shape or curvature of band 3 depending on the type of offset. While an offset of the Ge shell in X will maximally change the average AANR wavelength by 2.6%, and an offset in XYZ will maximally alter average AANR wavelength by 3.4%, these percentages translate to a change in AANR position of hundreds of nanometers, which can be significant when dealing with a narrow characterization region, though the AANR region still exists.

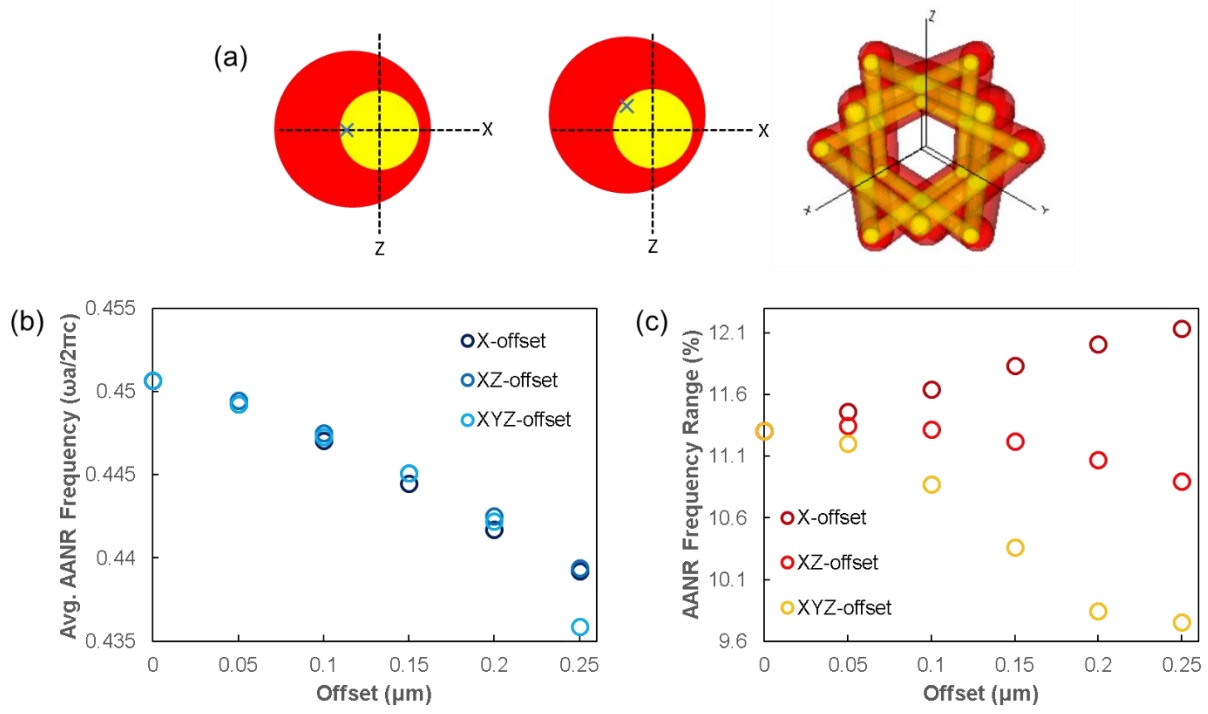

Figure S3. Examples of Ge-shell offset from the polymer-core center position in the X, XZ, and XYZ dimensions, and the effects of shell offset on average AANR Frequency and AANR Frequency range. (a) Schematics depicting the cross-section of a core-shell beam when the Ge-shell of offset from the center position of the polymer in the X-direction, XZ-directions, and XYZ-

directions. Note that the blue cross represents the new center position of the full beam following shell offset. (b) Average frequency at which AANR is observed in the PhC when shell-offset position is varied in 1, 2, and 3 dimensions. (c) AANR frequency range, represented as a percentage difference, for PhCs with varying shell-offset in X, XZ, and XYZ.

Methods

***Sample Fabrication*:** Nanolattices were first fabricated out of the acrylate-based "IP-Dip" photosensitive monomer, using a direct laser writing two-photon lithography (DLW TPL) system developed by Nanoscribe GmbH. For this DLW TPL process, the 3D periodic cube-like bcc architecture was created using a computer aided design (CAD) program which allowed for the generation of beams possessing nearly circular cross-sections. The design was then imported as a set of points describing the full 3D architecture to NanoWrite, proprietary software which interfaces with the Nanoscribe TPL DLW instrument to write the structure. To allow for subsequent optical characterization with an infrared laser of ~75-100μm spot size, lattices were designed to be 33 x 23 x 18 unit cells in x-y-z extent, resulting in structures with dimensions of approximately 130μm x 130μm x 100μm.

Nanolattice PhC samples were prepared by drop-casting the negative-tone photoresist "IP-Dip" (Nanoscribe GmbH) on a 500μm thick double sided polished silicon chip, to allow for transmission measurements through the sample and substrate. After exposing the photoresist and generating the 3D polymer scaffold, structures were developed for 30 minutes in propylene glycol mono-methyl ether acetate (PGMEA) followed by a 5-minute rinse in isopropyl alcohol. To prevent lattice collapse or excessive shrinkage due to capillary forces during the drying stage, lattices were dried via a critical point drying method using a Tousimis Autosamdri-815B, Series B critical point dryer.

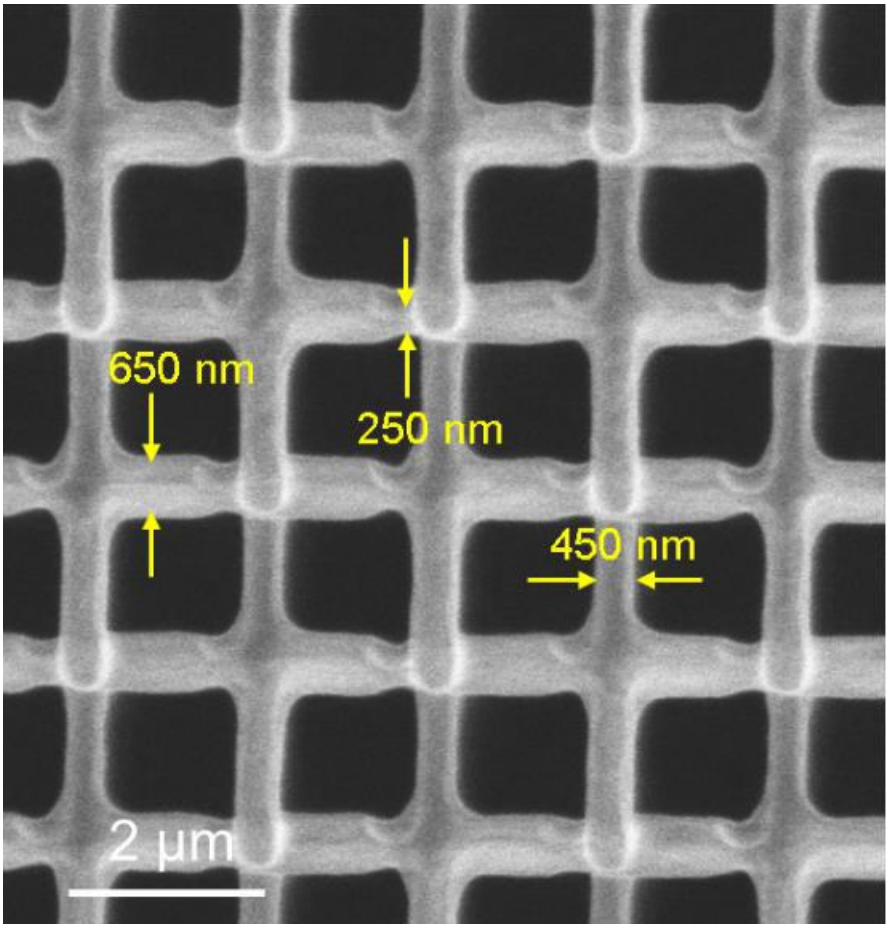

Figure S4. Scanning electron microscopy image of the $(10\bar{1})$ lattice face of a bcc PhC lattice after 45 min of oxygen-plasma etching. The electron microscope image is taken at a 45° tilt with approximate beam dimensions labeled in yellow.

Following fabrication with TPL DLW, lattices possess circular beams with dimensions on the order of ~850-900 nm. Using simulation results as a guide, we know it is necessary to reduce the polymer beam diameter to <600 nm. Lattices were dry etched with O_2 plasma using a Pie Scientific Tergeo Plus Plasma Cleaner in remote plasma cleaning mode. Typical etching conditions included an oxygen flow rate of 15 sccm and 50 W power. In downstream or remote plasma cleaning mode, oxygen plasma is generated outside sample chamber, which limits sample immersion in energetic plasma and reduces the extent to which lattices are sputtered by energetic ions. Through this process, only gentle, isotropic chemical etching should take place on the lattice beam surface by neutral radicals. Using these plasma etching parameters, we observed an average

beam etch rate of 10 nm/min. However, at high pressures, even these mild etch conditions caused anisotropic etching, resulting in the formation of elliptical beams as well as regions of over-etching which could be approximated as tapering (Figure S1).

The next step in the fabrication process for low-index core, high-index shell bcc PhC lattices is the deposition of germanium onto the etched polymer scaffold. We deposit germanium onto etched polymer lattices by sputtering with a germanium target (Kurt Lesker, Inc.) using a RF power supply at 100 W, under 5 mTorr and 20 sccm argon in a magnetron sputter deposition system (ATC Orion sputtering system, AJA International, Inc.). Base pressure is set to $<4\times10^{-6}$ Torr, and target ramp up and ramp down times are precisely controlled at 10 W/min to prevent the target from cracking. Prior to deposition on the sample, the target undergoes a 2-minute burn-in process to remove contaminates and surface oxide. To improve the conformality of Ge deposition and ensure material penetration through the lattice, sputtering was performed on samples mounted at 90° on an SEM stub on the rotating chuck. With this configuration, the side faces of the lattice, namely the (010) and $(10\bar{1})$ surfaces, were directed towards the target, rather than the lattice top. With the above mentioned sputtering parameters, we observed a deposition rate of 0.375 nm/min on the 3D lattice structure. Each of the four sample side faces were directed towards the target and sputtered in increments of 2hrs and 46min, resulting in the deposition of approximately 250 nm thick Ge shells on the polymer lattice beams.

Many polymers begin to degrade around 300 ^{o}C as shown by thermogravimetric analysis (TGA), which may lead to concern of degradation of the polymer. Specifically, for IP-Dip, thermogravimetric analysis (see Figure 7b in Supporting Information of reference 3) shows negligible loss of polymer in inert environment until above 400 ^{o}C.[3,4] At the high powers used in two-photon lithography to crosslink IP-Dip, the polymer is sufficiently highly cross-linked such

that the deformation and degradation temperatures should occur at roughly the same temperature. As a result, we do not expect deformation or degradation of the polymer due to this sputtering process.

In this work, sputter coating was chosen due to limitations in available deposition techniques for Ge. Sputtering is a physical deposition process, which is difficult to optimize for a 3D architecture and may lead to non-conformalities or non-uniformities. It is worth noting that with sputter coating, as the total beam thickness becomes larger, the structure is less open, meaning that deposition deep into the lattice becomes more and more difficult. Should other chemical deposition techniques be available (e.g. atomic layer deposition or chemical vapor deposition) for high index materials, this could greatly improve the deposition around the beams and reduce experimental fabrication imperfections. While the primary concern is the effective index between the polymer core and the high-index Ge shell, fabrication of these structures can be greatly facilitated with a more consistent chemical deposition technique.

Focused ion beam (FIB) milling was used to assess the conformality and thickness of Ge deposited onto polymer lattices. To be as minimally destructive towards the sample, only the edges of the core-shell PhC were FIB milled, revealing beam cross-sections for imaging and measurement with scanning electron microscopy (SEM). Such cuts are approximately 10 μm wide and span the height of the lattice, so that deposition can be assessed through all z-layers. We examine Ge deposition and beam dimensions as a function of depth by iteratively FIB milling through the lattice. We measure an average lattice period of 3.8 μm, likely from structure shrinkage during TPL DLW. Subsequent cuts into the lattice reveal that offset in Ge shell/polymer core position persists through the beam length, and dimensions of the full beam and polymer core do not vary significantly, remaining elliptical with similar average dimensions as described. FIB

cross-sectioning reveals that the Ge shell is conformal but non-uniform. An average of the polymer core dimensions compared to the full core-shell beam dimensions provides determination of an average Ge shell thickness of 255 nm, sufficient for observation of NR.

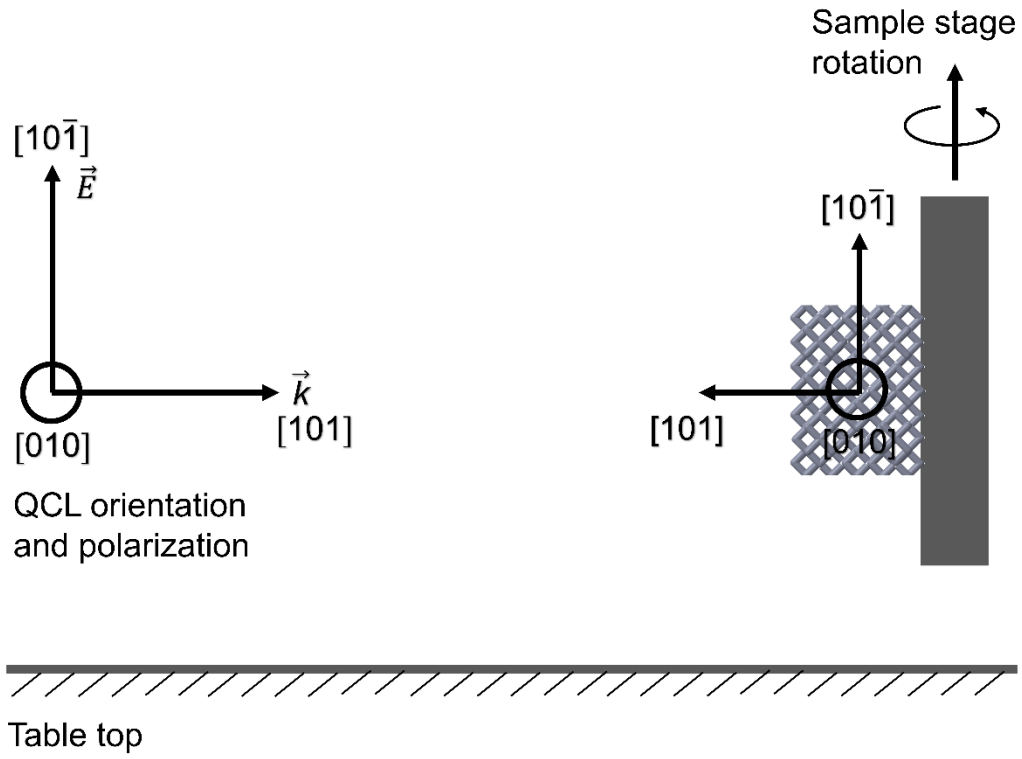

Figure S5. Schematic of a side view of the experimental measurement set-up showing the orientation of incident QCL laser light relative to the PhC sample orientation. It should be noted that incident light is polarized along the [10$\bar{1}$] direction.

***Measurement*:** Angle resolved spectroscopic measurements to selectively excite states at precise momentum and wavelength is done in a setup consisting of a quantum cascade laser (QCL) with an operating mode between 7.7-8.62 μm as the source, a series of ZnSe lenses to focus the laser beam down to spot size approximately 100 μm in diameter, and a germanium beam splitter to direct half of the laser beam to a reference detector, and half to the sample (Figure S2). Pyroelectric sample and reference detectors are mounted on concentric rotation stages allowing for the collect

of transmission and reflection spectra at distinct angles of incidence. Alignment of the laser beam and the PhC sample is accomplished using a visible CCD camera and alignment markers. More precise micron scale alignment is performed by transmitting QCL light through the sample, and projecting the magnified image onto a mid-IR camera with MCT detector to determine sample edges versus the sample center.

Measurements are taken between $\theta = 22.5°$ to 45°. Below 22.5º, limitations in the set-up (i.e. detector size) prevent measurements at smaller angles. In theory, measurements can be taken at angles greater than 45º, though the limited lateral area of the as-fabricated samples limits measurements at greater incident angles. Fabrication of larger lateral area lattices with similar feature sizes may require stitching in two-photon lithography.

Simulation Parameters for Comparison to Experimental Band Structure

Figure 3 compares the experimentally measured band structure to results generated in PWE. The simulated PhC in Figure 3b accounted for the structural features and lattice dimensions determined through FIB and SEM measurements. The unit cell size was set to 3.8μm, and beam ellipticity, taper, and Ge shell offset were all accounted for as follows. Beam ellipticity was accounted by approximating the polymer core as an elliptical beam with long axis and short axis dimensions of 650nm and 450nm, respectively. Taper was introduced to polymer beams pointing in the [010] direction by changing the long axis dimension of their starting vertex to 250nm and while keeping it at 650nm at the ending vertex, creating a core resembling an elliptical conical frustrum. The germanium shell was described by embedding the polymer core in an elliptical beam of Ge with long axis and short axis dimensions of 1.1 μm and 860 nm respectively. The Ge shell beams were also offset from the polymer core beams by 200 nm in x, y, and z, yielding a representative core-shell PhC for simulation. We then calculate the band structure for this PhC

approximation in the frequency range between $\omega = 0.441(2\pi c/a)$ and $\omega = 0.494(2\pi c/a)$ and angular span between 22.5° to 45° along the ΓN direction.

REFERENCES

(1) Chernow, V. F.; Ng, R. C.; Greer, J. R. Designing Core-Shell 3D Photonic Crystal Lattices for Negative Refraction. *Proc. SPIE* **2017**, 10112.

(2) Meza, L. R. Design, Fabrication, and Mechanical Property Analysis of 3D Nanoarchitected Materials. California Institute of Technology, 2010.

(3) Liu, Y.; Wang, H.; Ho, J., Ng, R. C.; Ng, R. J. H.; Hall-Chen, V. H.; Koay, E. H. H.; Dong, Z.; Liu, H.; Qiu, C-W.; Greer, J. R.; Yang, J. K. W. Structural Color Three-Dimensional Printing by Shrinking Photonic Crystals. Nature Comm. 2019, 10, 4340.

(4) Sharipova, M. I.; Baluyan, T. G.; Abrashitova, K. A.; Kulagin, G. E.; Petrov, A. K., Chizhov, A. S.; Shatalova, T. B.; Chubich, D.; Kolymagin, D. A.; Vitukhnovsky, A. G.; Bessonov, V. O.; Fedyanin, A. A. Effect of Pyrolysis on Microstructures Made of Various Photoresists by Two-Photon Polymerization: Comparative Study. Opt. Mater. Express 2021, 11, 371-384